

Tuning the chiral orbital currents in a colossal magnetoresistive nodal line ferrimagnet

Arnab Das and Soumik Mukhopadhyay*

Department of Physics, Indian Institute of Technology Kanpur, Kanpur 208016, India

The ferrimagnetic nodal-line semiconductor $\text{Mn}_3\text{Si}_2\text{Te}_6$ exhibits colossal magnetoresistance (CMR) owing to the chiral orbital currents (COC). The COC is developed due to spin-orbit interaction (SOI) attributed to the tellurium (Te) atoms. Here, we observe that on chemical substitution of the Te atoms with selenium (Se), the COC, which runs along the Te-Te edges of the MnTe_6 octahedra, becomes weaker and thus affects the angular magnetoresistance (MR) of $\text{Mn}_3\text{Si}_2\text{Te}_6$. We find that the application of magnetic field along the easy axis leads to a considerable drop in resistance in substituted crystals, which otherwise exhibits weak MR. On the other hand, the CMR effect along the partially polarized magnetization direction is found to be only marginally affected due to the substitution and persists even for a significantly high concentration of Se.

Introduction:— The phenomena of colossal magnetoresistance (CMR) is not new and have been under study since the 1990's when it was first discovered in a hole-doped perovskite system [1–12]. In such systems, the CMR is governed by the interplay of double exchange mechanism and dynamic Jahn-Teller effect which plays a key role in bringing forth the concurrent magnetic and metal-insulator transition [13–16]. Later on, however, materials like $\text{Ti}_2\text{Mn}_2\text{O}_7$ [17, 18], $\text{Eu}_5\text{In}_2\text{Sb}_6$ [19], EuCd_2P_2 [20], EuTe_2 and EuMnSb_2 [21–23], have been discovered that shows CMR without following the conventional mechanism typical of doped perovskites. In recent times, two-dimensional (2D) layered correlated systems with transition atoms have gained much attention due to their rich physical properties, including CMR [24]. In layered ferrimagnetic (FIM) nodal-line semiconductor $\text{Mn}_3\text{Si}_2\text{Te}_6$, a very large CMR is exhibited which forces the resistivity to drop by several orders of magnitude. However, this sharp decrease in resistance occurs only when the magnetic field is applied along the magnetic hard axis [25, 26]. Thus, the CMR in $\text{Mn}_3\text{Si}_2\text{Te}_6$ is not dictated by the spin polarization. Rather, it occurs only when the spin polarization is avoided [27]. This CMR is quite unique and shows a current dependency, decreasing with the increase in current, and finally vanishes at a particular threshold current, I_C [28]. The origin of this unique CMR in $\text{Mn}_3\text{Si}_2\text{Te}_6$ has been attributed to the breaking of nodal-line degeneracy. The spin-orbit coupling (SOC) between Mn and Te shifts one of the bands towards the Fermi level, inducing a metal-insulator transition when the field is along the out-of-plane (OOP) direction [25, 29, 30]. An alternative perspective focuses on the chiral-orbital currents (COC) that flow along the Te edges in the ab-plane of $\text{Mn}_3\text{Si}_2\text{Te}_6$. These currents generate a moment, M_{COC} , along the c-axis, which couples with the moments of the Mn atoms, M_{Mn} . When the magnetic field is along the c-axis, the combined effect of M_{COC} and M_{Mn} governs the observed magnetization and CMR effect [28, 31–33]. However, till now, most of the interesting phenomena about $\text{Mn}_3\text{Si}_2\text{Te}_6$ have been found along the c-axis only, which surprisingly is not the magnetic easy axis. There have been very few reports about the properties of $\text{Mn}_3\text{Si}_2\text{Te}_6$ along the easy plane (the ab-plane), exacerbated by the fact that in the ab-plane, the magnetoresistance (MR) is low. Thus, further research to improve the MR

response along the magnetic easy plane and connecting it with the existing theories is crucial to draw a complete picture of the physics of $\text{Mn}_3\text{Si}_2\text{Te}_6$ and also for future applications.

In our work, we observe that by progressive substitution of the tellurium with selenium, the negative MR along the ab-plane increases. Additionally, this substitution has very little effect on the already high CMR observed along the c-axis. Our calculations reveal that the MR behaviour of $\text{Mn}_3\text{Si}_2\text{Te}_6$ is deeply linked with the magnetisation anisotropy and the resulting modification of COC.

Crystal Growth:— Single crystals of $\text{Mn}_3\text{Si}_2\text{Te}_6$ have been prepared using the chemical vapour transport (CVT) method [34] where iodine is used as the transport agent. The initial precursors, Mn (99.95%, Alfa Aesar), Si (99.999%, Alfa Aesar), and Te (99.99%, Alfa Aesar) powders, are mixed in the stoichiometric ratio of 3:2:6. The powders are homogeneously mixed and pelletized, and then kept in a vacuum-sealed quartz ampoule along with 40 mg of I_2 . The growth process utilizes a TG3-1200 gradient three-zone tube furnace with the hot end kept at 800°C and the cold end maintained at 750°C. Both ends are heated at a rate of 60°C/hr. The ampoule is kept in the furnace for 20 days, and after that, it is cooled to room temperature and taken out. The result is the formation of crystals of 1-2 mm in size.

For substituting tellurium (Te) by selenium (Se) with different concentrations, we employ similar CVT technique. Here, Mn (99.95%, Alfa Aesar), Si (99.999%, Alfa Aesar), Te (99.99%, Alfa Aesar) and Se (99.999%, Alfa Aesar) powders, are mixed in the stoichiometric ratio. Again, the mixture is pelletized and kept in an ampoule and placed in the three-zone furnace. This time, the hot zone is kept at 750°C and the cold end at 700°C and the ampoule is kept in the furnace for 17 days. Upon cooling to room temperature, we successfully obtain the crystals.

Characterization:— X-ray diffraction (XRD) and energy dispersive spectroscopy (EDS) measurements are performed to determine the crystallinity as well as the elemental composition of both the substituted and unsubstituted sample. The stoichiometry of all the samples is confirmed from the EDS measurements. Fig.-1(a)-(e) presents the EDS spectra with prominent Mn, Si, Te and Se peaks, obtained from freshly cleaved surfaces of $\text{Mn}_3\text{Si}_2(\text{Te}_{1-x}\text{Se}_x)_6$ single crystals for

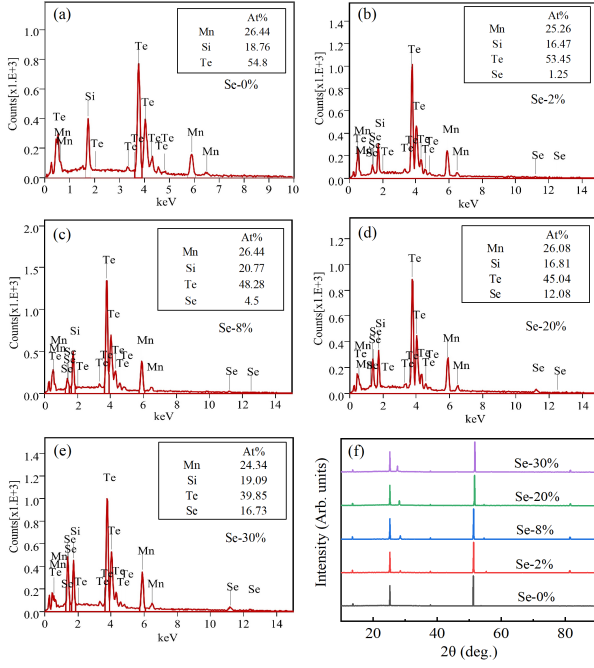


FIG. 1: (a) - (e) Energy dispersive spectroscopy data of $\text{Mn}_3\text{Si}_2(\text{Te}_{1-x}\text{Se}_x)_6$ single crystals for different values of x . (f) XRD Data of $\text{Mn}_3\text{Si}_2(\text{Te}_{1-x}\text{Se}_x)_6$ single crystals for different values of x .

different x values. The atomic percentage is also highlighted in the inset for each grown crystal, which confirms that the obtained stoichiometry is close to the targeted one. The X-ray diffraction (XRD) measurement is carried out using a PANalytical X'Pert diffractometer to confirm the high crystallinity of the grown crystals. Fig-1(f) shows the XRD data of the as grown single crystals for different x values, which reveal the (001) orientation of the crystal surface. The temperature dependence of magnetization and the isothermal magnetization hysteresis measurements have been carried out using a Quantum Design physical properties measurement system (PPMS). The electrical transport properties have been measured in a CRYOGENIC variable temperature insert (VTI) cryostat using the standard lock-in technique.

Results and Discussion:— The bulk magnetization data for Se-0% has been plotted in Fig-2. It shows that bulk $\text{Mn}_3\text{Si}_2\text{Te}_6$ single crystal has a Curie temperature $T_C \sim 78$ K, which is consistent with previous reports [25–28, 31, 35, 36]. The inset of Fig-2 shows the variation of T_C with selenium concentrations. It is clearly seen that with increasing selenium concentration, the T_C decreases from 79 K to 69 K as Se substitution level reaches 30%.

Since the resistivity of $\text{Mn}_3\text{Si}_2(\text{Te}_{1-x}\text{Se}_x)_6$ varies with different applied currents [28], all electrical transport measurements have been performed at a fixed current of $I = 100$ nA to avoid any current-induced effect on our observed results. Fig.-3(a) - (d) shows the temperature dependence of resistivity at different magnetic fields, along the ab-plane and c-axis,

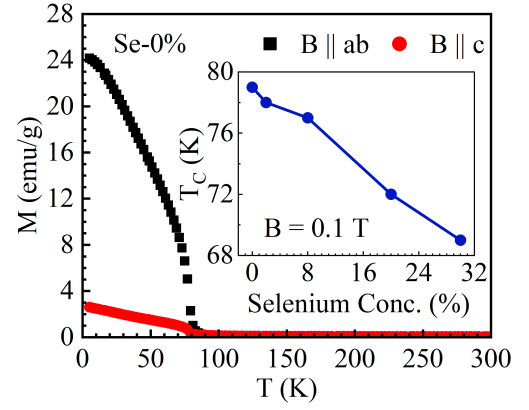


FIG. 2: Temperature dependence of magnetization $M(T)$ of Se-0% single crystal at an applied field of $B = 0.1$ T with both $B \parallel ab$ and $B \parallel c$ directions. Inset: Variation of Curie temperature T_C with selenium concentration.

for both Se-0% and Se-8% samples, respectively. The zero-field (ZF) (with $B = 0$ T) longitudinal resistivity ρ_{xx} , for both the samples, increases rapidly as we decrease the temperature, which indicates their semiconducting nature. The most remarkable feature of the Se-0% sample is the CMR along the c-axis, as can be seen in Fig.-3(b). Here, the resistivity sharply drops by 10^3 of magnitude when $B \parallel c$. However, from Fig.-3(a), we can see that such huge drop in resistivity is completely absent when $B \parallel ab$. On the other hand, for Se-8% sample, as shown in Fig.-3(c), there is a significant drop in ρ_{xx} even when $B \parallel ab$, without significantly affecting the drop along $B \parallel c$. To dig further into this contrasting behaviour of ρ_{xx} for Se-0% and Se-8% samples, we perform the magnetoresistivity (MR) measurements of all the samples.

Fig.-3(e) and Fig.-3(f) shows the temperature dependence of MR ($\Delta\rho/\rho(0)$) for different values of x along the ab-plane and the c-axis, respectively. Here, $\frac{\Delta\rho}{\rho(0)} = \frac{\rho(B) - \rho(0)}{\rho(0)}$ where $\rho(B)$ is the longitudinal resistivity measured at an applied magnetic field of B , and $\rho(0)$ is the ZF longitudinal resistivity. We find that when $B \parallel ab$, for any temperature below 100 K, the value of $\Delta\rho/\rho(0)$ becomes more and more negative as we increase the selenium concentration. Above 100 K, the MR values along both field directions become negligible due to the absence of magnetic long range order.

Next, we perform the MR measurements at constant temperatures for all values of x . The MR% is then calculated and is shown in Fig-4 with $B \parallel c$ (Fig-4(a)-(d)), and $B \parallel ab$ (Fig-4(e)-(h)), respectively. Here the MR% is calculated as, $\text{MR}\% = \frac{\Delta\rho}{\rho(0)} \times 100$. For $x = 0$, we see that the CMR is present only along the c-axis and gets more pronounced with decreasing temperature. At 20 K, the MR% reaches almost -98% when $B \parallel c$, as is evident from Fig-4(a). However, as can be seen in Fig-4(e), the CMR vanishes when the direction of the magnetic field is changed along the ab-plane. For $B \parallel ab$, even at low temperatures of 20 K, the resistance drop is comparatively small $\sim -15\%$. As x is increased, the CMR effect

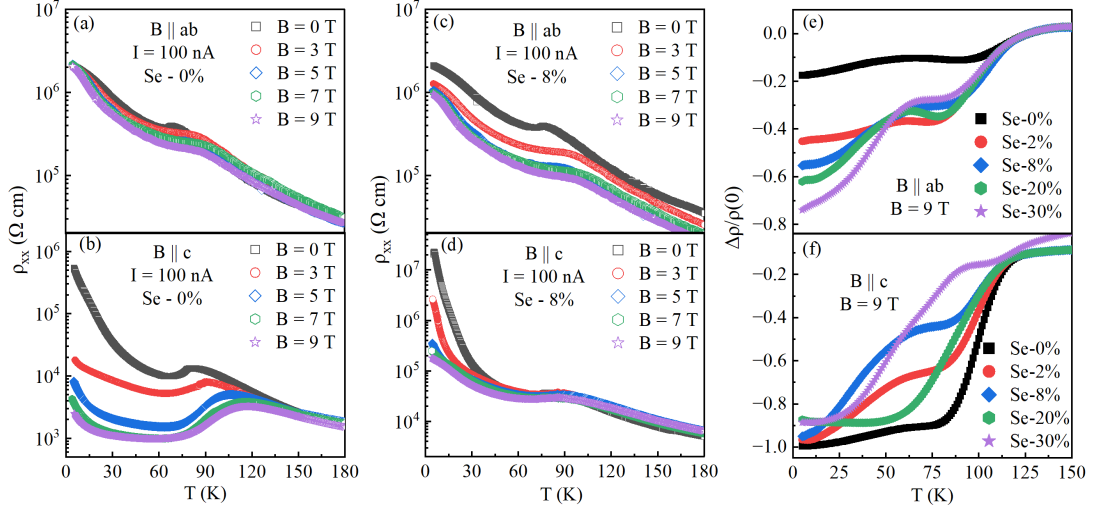


FIG. 3: Temperature dependence of longitudinal resistivity ρ_{xx} of Se-0% crystal measured at constant magnetic fields with (a) $B \parallel ab$ and (b) $B \parallel c$. Temperature dependence of longitudinal resistivity ρ_{xx} of Se-8% crystal measured at constant magnetic fields with (c) $B \parallel ab$ and (d) $B \parallel c$. Temperature dependence of magnetoresistivity $\Delta\rho/\rho(0)$ of $\text{Mn}_3\text{Si}_2(\text{Te}_{1-x}\text{Se}_x)_6$ single crystals with (e) $B \parallel ab$ and (f) $B \parallel c$, measured at 9 T.

along the c-axis persists for all chemically substituted levels.

The MR curves along the ab-plane are plotted in Fig.-4(e)-(h) for all $x \neq 0$. At a low temperature of 20 K, the maximum value of MR is $\sim -15\%$, for $x = 0$. However, for the Se-2% substituted samples, the same is $\sim -45\%$, and for Se-8%, Se-20% and Se-30% the values drop down to -55%, -60% and -69%, respectively. Thus, the negative MR increases with the concentration of Se when the field is applied along the ab-plane. This is strikingly different to what happens when the field direction is along the c-axis. The increased magnitude of negative MR for $B \parallel ab$ in substituted samples is not only limited to lower temperatures but can be seen to persist even at temperatures marginally higher than the transition temperature.

To get more insight into this peculiar MR behaviour, the isothermal magnetization measurements were performed on all the samples. Fig.-5 shows the isothermal magnetization curves for different values of x with the field applied along both the ab-plane and c-axis, respectively. It can be seen from Fig.-5(a) that when the direction of the magnetic field is along the ab-plane, the saturation magnetization M_s (at $B = 7$ T) increases with the increase in selenium concentration. This situation, however, reverses when the field direction is along the c-axis. For $B \parallel c$, the magnetization does not saturate at high fields of 7 T owing to the high magnetic anisotropy in the system, which persists even after selenium substitution. Moreover, Fig.-5(b) clearly shows that the magnetization M (at $B = 7$ T) along the c-axis decreases as the selenium concentration is increased.

The inset of Fig.5(a) shows a schematic illustration of the density of states (DOS) for both the unsubstituted and substituted crystals. The blue and green bands refer to the Mn1

and Mn2 states, respectively. The broader yellow bands represent Tellurium or Selenium. The Mn1 and Mn2 spin states in Fig.-5(a).(i) points opposite to each other, indicating the FIM state. However, in Fig.-5(a).(ii), they lie in the same direction indicating an FM state [25]. For a hypothetical FM state, the band gap gets closed and thus, in Fig.-5(a).(ii), the yellow band is slightly elongated to illustrate this band closing. Now, as is evident from Fig.-5(a), when the concentration of selenium is increased, the magnetization saturates almost instantly with the applied field. This indicates that, as we increase the concentration of selenium, the ferrimagnetic $M(B)$ curve becomes more ferromagnetic in nature. Comparing this with Fig.-5(a).(ii) we conclude that when $B \parallel ab$, the band gap closes as we increase the selenium concentration. However, the magnetization behaviour along the c-axis is opposite to what we observe along the ab-plane.

This contrasting magnetization behaviour along different directions of the applied magnetic field can be attributed to the COC developed in $\text{Mn}_3\text{Si}_2(\text{Te}_{1-x}\text{Se}_x)_6$ crystals due to the Te atoms. It is well known that the COC that circulates along the Te edges produces a magnetic moment M_{COC} of its own which orients along the c-axis as the orbital currents flow along the ab-plane [28]. Thus, the net magnetic moment is a combination of both M_{COC} and the moments arising from the Mn atoms, M_{Mn} . For unsubstituted $\text{Mn}_3\text{Si}_2\text{Te}_6$ crystal, the Mn atoms (M_{Mn}) predominantly point along the ab-plane unlike M_{COC} which points along the c-axis. The coupling between the M_{COC} and M_{Mn} gives rise to a unique SOC effect, which on the application of magnetic field underpins the CMR in the Se-0% sample [25, 28]. Thus, the saturation magnetization and CMR are interlinked with each other. Substituting the tellurium site of $\text{Mn}_3\text{Si}_2\text{Te}_6$ with selenium decreases the

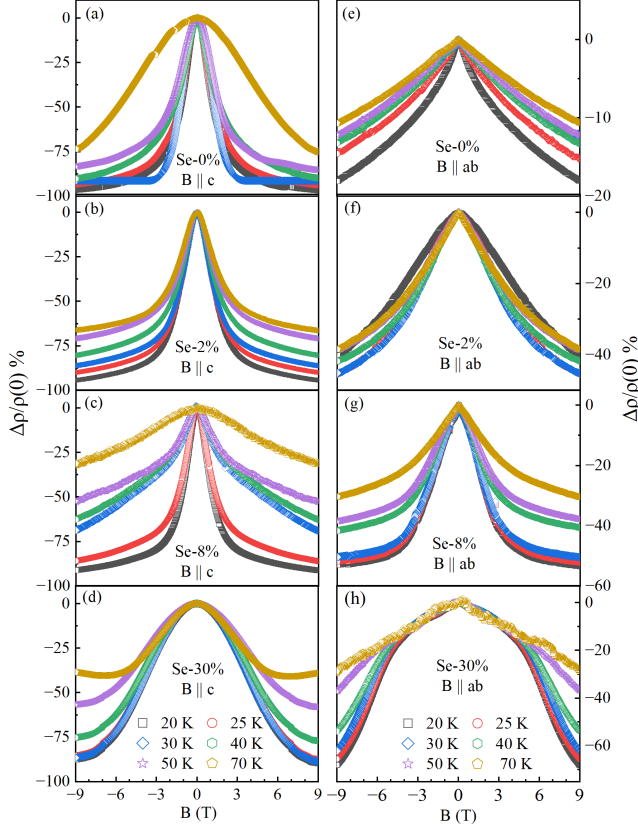


FIG. 4: (a) - (d) Magnetic field dependence of MR for $\text{Mn}_3\text{Si}_2(\text{Te}_{1-x}\text{Se}_x)_6$ at various temperatures with $B \parallel c$. (e) - (h) Magnetic field dependence of MR for $\text{Mn}_3\text{Si}_2(\text{Te}_{1-x}\text{Se}_x)_6$ at various temperatures with $B \parallel ab$. The applied bias current is $I = 100$ nA for all measurements.

orbital currents and its corresponding domain area decreases as selenium is smaller in size than tellurium. Thus, the orbital moment contribution M_{COC} arising due to the COC of tellurium become smaller with increasing selenium substitution. So the coupling between M_{COC} and M_{Mn} becomes weaker with increasing concentration of selenium. Thus, the net magnetic moment of the substituted $\text{Mn}_3\text{Si}_2(\text{Te}_{1-x}\text{Se}_x)_6$ crystals is dominated by the Mn atoms in contrast to the unsubstituted crystal. Due to this decreased coupling between M_{COC} and M_{Mn} , the SOC developed due to the combined effect of both gets reduced, leading to the MR and the magnetization behaviour of the substituted crystals as observed in Fig.-4 and Fig.-5.

Fig.-6 simultaneously shows the saturation magnetization M_s , effective anisotropy constant K_{eff} and maximum negative MR as a function of selenium concentration x in both in-plane (IP) and out-of-plane (OOP) configurations, respectively. The K_{eff} has been calculated by fitting the isothermal magnetization data in Fig-5 with an empirical model for the M-B curve for different x values along both field directions. The $M(B)$ measurements for all the samples were recorded

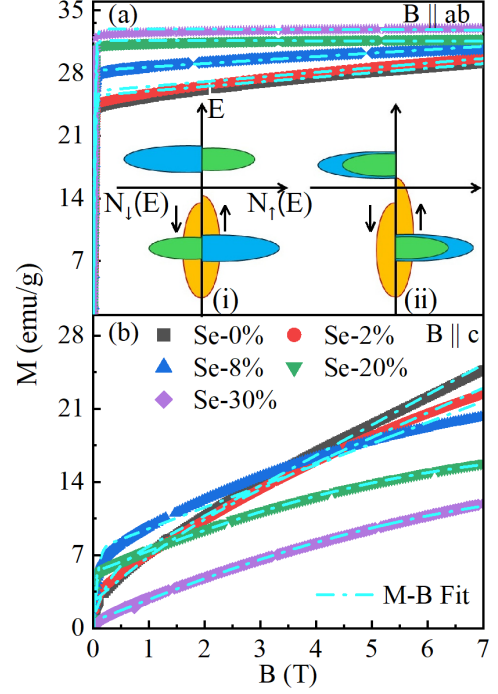


FIG. 5: Isothermal magnetization $M(B)$ of $\text{Mn}_3\text{Si}_2(\text{Te}_{1-x}\text{Se}_x)_6$ single crystals for different concentrations of selenium with (a) $B \parallel ab$ and (b) $B \parallel c$ directions, respectively. The $M(B)$ curves are fitted using an empirical model discussed in the text. The dash-dot lines represent the fitted curves. Inset: Schematic illustration of the spin density of states (DOS) for both (i) the unsubstituted and (ii) substituted crystals. Here, blue represents the Mn1 states, green represents the Mn2 states and yellow represents the Te/Se states.

using a five-quadrant measurement. The curves show almost negligible hysteresis, and thus, only the positive cycle of the $M(B)$ curves are shown in Fig.-5. Our analysis shows that COC plays a crucial role in governing the magnetization and MR behaviour of all the samples. Hence, to find the causal relation between COC and selenium substitution, we need to get an idea of the strength of the SOC for all the samples. Qualitatively, the behaviour of K_{eff} is analogous to the behaviour of SOC. Thus, calculating the variation of K_{eff} with the selenium concentration will give us a clear picture of the behaviour of SOC with the same. The following analysis is based on the Stoner-Wolarth model and the Law of Approach to Saturation [37–41].

According to the Stoner-Wolarth model, the total energy E of a ferromagnet is given by:

$$E = K_{\text{eff}} V \sin^2 \theta - M_s B V \cos(\theta - \phi) \quad (1)$$

where K_{eff} = effective anisotropy constant, V = volume of the particle, M_s = saturation magnetization, B = applied magnetic field, θ = angle of magnetization with respect to the easy axis, and ϕ = angle of the applied field with respect to the easy axis. Based on this model, the descending branch of $M(B)$ curve at

high fields can be approximated by:

$$|M| = M_s \left[1 - \frac{H_K^2}{C \cdot B^2} \right] \quad (2)$$

where C is a constant depending upon the system, and $H_K = 2K_{\text{eff}}/M_s$. This is called the Law of Approach to Saturation [37, 38]. Based on the above two equations, the expression for fitting the entire $M(B)$ curve is given by [38]:

$$\frac{M}{M_s} = g(B)f(\xi, 0) + (1 - g)f(\xi, \infty) \quad (3)$$

where,

$$f(\xi, 0) = \coth\left(\frac{BM_s}{k_B T}\right) - \frac{k_B T}{BM_s} \quad (4)$$

$$f(\xi, \infty) = a_1 \tanh\left(b_1 \frac{BM_s}{k_B T}\right) + a_2 \tanh\left(b_2 \frac{BM_s}{k_B T}\right) + a_3 \tanh\left(b_3 \frac{BM_s}{k_B T}\right) \quad (5)$$

$$g(B) = c_1 \tanh\left(d_1 \frac{B}{H_K}\right) + c_2 \tanh\left(d_2 \frac{B}{H_K}\right) + c_3 \tanh\left(d_3 \frac{B}{H_K}\right) \quad (6)$$

Here, a_i , b_i , c_i and d_i are all constants with $i = 1, 2$, and 3 , k_B is the Boltzmann constant and T is temperature. We use Eqn.-(3) for fitting the $M(B)$ curves along both field directions.

It can be seen from Fig.-6(a) that on increasing selenium concentration x , the saturation magnetization M_s^{ab} (along ab-plane) increases and so does the negative MR%. However, the effective anisotropy constant K_{eff} reduces with increasing selenium concentrations. Qualitatively, a decrease in the effective anisotropy indicates a decrease in the overall SOC. Thus, we can deduce that the SOC induced due to the heavy Te atoms gets reduced when it is substituted with lighter Se atoms. Fig.-6(a) shows a correlation between the saturation magnetization and the MR response, indicating that one behaviour is influenced by the other. It is evident that selenium substitution leads to a higher value of saturation magnetization M_s^{ab} . Since the observed magnetization is a combined effect of M_{COC} and M_{Mn} , a higher magnetization value indicates a weaker cancellation effect between the M_{COC} and M_{Mn} .

When the field is along the ab-plane, the Mn moments readily point along the applied field as it is the easy plane. For the Se-0% sample, the M_{COC} points along the c-axis only, as the COC predominantly circulates along the ab-plane itself. The generated COC domains are much smaller and decrease further with an increase in the magnetic field. For the Se-0% sample, the magnetization does not readily saturate at smaller field values since the COC domains do not completely vanish. Thus, the effective magnetic moment along the ab-plane is

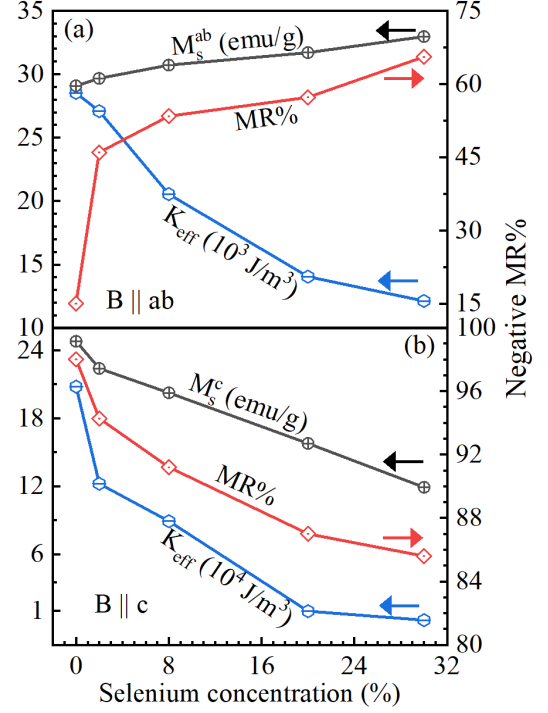


FIG. 6: Saturation magnetization M_s (at $B = 7$ T), effective anisotropy constant K_{eff} and maximum negative MR% (at $B = 9$ T) as a function of selenium concentrations x with (a) $B \parallel \text{ab}$ and (b) $B \parallel \text{c}$ directions respectively. The saturation magnetization and effective anisotropy constant are plotted along the left y-axis with black and blue symbols, respectively. On the right y-axis, the negative MR% is plotted with red symbols. The continuous lines act as a guide to the eye.

somewhat less than what it should have been if there had been no M_{COC} along the c-axis. As we substitute tellurium with selenium, the small COC domains shrink. The effective moment increases with the increasing concentration of selenium, and the FIM state eventually becomes FM, as can be seen from Fig.-5(a). The reduction in M_{COC} also decreases the SOC along the ab-plane, as is evident from Fig.-6(a). With the decreasing SOC and the strengthening of FM character, the DOS of the substituted samples closes the band gap as is illustrated in Fig.-5(a).ii). Hence, more electrons become available for conduction for the substituted samples. Thus, we can see a simultaneous increase in both effective moment and negative MR along the ab-plane with increasing selenium substitution.

For $B \parallel \text{c}$, all the three curves of M_s^{c} , negative MR% and K_{eff} follow similar behaviour as we increase the selenium concentration which can be seen in Fig.-6(b). The striking similarity between the three curves in Fig.-6(b) again ascertains that with an increase in selenium concentration, the M_{COC} gradually decreases, which decreases the effective moment along the c-axis. The CMR also follows the same trend.

When the field is along the c-axis, depending on the field value (whether negative or positive), the COC circulates in ei-

ther a clockwise or anticlockwise direction, respectively. As the field is increased, the domain of a particular chirality is favoured, and it enlarges in size, which causes the moments of the same chirality, M_{COC} , to align collectively towards the field direction, thereby increasing the COC moments. Since the Mn atoms do not readily point along the c-axis, the M_{Mn} aligns along the field direction slowly with increasing field value. This leads to a coupling between M_{COC} and M_{Mn} that causes a sharp decrease in electron scattering [28] and thus promotes the negative CMR along the c-axis for Se-0% crystal. However, when selenium concentration is increased, the expansion of a single COC domain is impeded as selenium does not produce any COC. This leads to a reduction in the size of individual COC domains and decreases the COC moments M_{COC} . Thus, the sharp reduction in electron scattering is partially suppressed with increasing substitution, which leads to a decrease in the CMR effect but not its complete disappearance as the COC domains of the remaining Te atoms still cause sufficient reduction in electron scattering which paves the way for CMR. Thus the contrasting behaviour of M_s and negative CMR on changing the direction of the applied field in Fig.-6 points to the fact that the entire scenario is governed by COC moments, which has opposite effects along the two crystallographic axes.

Conclusion:— We have studied the magnetization and electrical transport properties of FIM nodal-line semiconductor $\text{Mn}_3\text{Si}_2(\text{Te}_{1-x}\text{Se}_x)_6$ as a function of substitution concentrations. We observe that as we substitute the tellurium (Te) with selenium (Se), the COC domains decrease in size. This leads to a decrease in the moment induced by the COC (M_{COC}) and subsequently coupling between M_{COC} and M_{Mn} , which has opposite effects along the ab-plane and c-axis, respectively. The ab-plane magnetization, as well as the negative MR, increases as we increase the concentration of selenium, and the isothermal magnetization curves of the selenium substituted samples show a much more FM character than the FIM unsubstituted sample. On the other hand, the c-axis magnetization and the CMR tends to decrease, albeit marginally, with increasing chemical substitution. Thus, our findings reveal the close relationship between magnetization and CMR. By chemical substitution of tellurium of $\text{Mn}_3\text{Si}_2\text{Te}_6$, we are able to increase the negative MR along the ab-plane without hindering much the CMR effect along the c-axis, which could be potentially useful for applications.

Acknowledgements:— The authors acknowledge IIT Kanpur and the Department of Science and Technology, India, [Order No. DST/NM/TUE/QM-06/2019 (G)] for financial support. A.D. thanks PMRF for financial support.

* Electronic address: soumikm@iitk.ac.in

[1] R. M. Kusters, J. Singleton, D. A. Keen, R. McGreevy, and W. Hayes, Magnetoresistance measurements on the magnetic semiconductor $\text{Nd}_{0.5}\text{Pb}_{0.5}\text{MnO}_3$, *Physica B: Condensed Matter*. **155**, 362-365 (1989).

[2] R. von Helmolt, J. Wecker, B. Holzapfel, M. Schultz, and K. Samwer, Giant negative magnetoresistance in perovskitelike $\text{La}_{2/3}\text{Ba}_{1/3}\text{MnO}_x$ ferromagnetic films, *Phys. Rev. Lett.* **71**, 2331-2333 (1993).

[3] K. Chahara, T. Ohno, M. Kasai, and Y. Kozono, Magnetoresistance in magnetic manganese oxide with intrinsic antiferromagnetic spin structure, *Appl. Phys. Lett.* **63**, 1990-1992 (1993).

[4] S. Jin, T. H. Tiefel, M. McCormack, R. A. Fastnacht, R. Ramesh, and L. H. Chen, Thousandfold Change in Resistivity in Magnetoresistive La-Ca-Mn-O Films, *Science* **264**, 413-415 (1994).

[5] Y. Tokura, A. Urushibara, Y. Moritomo, T. Arima, A. Asamitsu, G. Kido, and N. Furukawa, Giant Magnetotransport Phenomena in Filling-Controlled Kondo Lattice System: $\text{La}_{1-x}\text{Sr}_x\text{MnO}_3$, *J. Phys. Soc. Jpn.* **63**, 3931-3935 (1994).

[6] A. Asamitsu, Y. Moritomo, Y. Tomioka, T. Arima, and Y. Tokura, A structural phase transition induced by an external magnetic field, *Nature* **373**, 407-409 (1995).

[7] A. Urushibara, Y. Moritomo, T. Arima, A. Asamitsu, G. Kido, and Y. Tokura, Insulator-metal transition and giant magnetoresistance in $\text{La}_{1-x}\text{Sr}_x\text{MnO}_3$, *Phys. Rev. B* **51**, 14103-14109 (1995).

[8] A. J. Millis, B. I. Shraiman, and R. Mueller, Dynamic Jahn-Teller Effect and Colossal Magnetoresistance in $\text{La}_{1-x}\text{Sr}_x\text{MnO}_3$, *Phys. Rev. Lett.* **77**, 175-178 (1996).

[9] H. Röder, J. Zang, and A. R. Bishop, Lattice Effects in the Colossal-Magnetoresistance Manganites, *Phys. Rev. Lett.* **76**, 1356-1359 (1996).

[10] A. P. Ramirez, Colossal magnetoresistance, *J. Phys.: Condens. Matter* **9**, 8171 (1997).

[11] J. M. D. Coey, M. Viret, and S. von Molnár, Mixed-valence manganites, *Adv. Phys.* **48**, 167-293 (1999).

[12] Y. Tokura, Colossal magnetoresistive oxides, CRC Press, 2000.

[13] M. B. Salamon and M. Jaime, The physics of manganites: Structure and transport, *Rev. Mod. Phys.* **73**, 583-628 (2001).

[14] E. Dagotto, Nanoscale Phase Separation and Colossal Magnetoresistance, Springer, Berlin, 2002.

[15] E. Dagotto, T. Hotta, and A. Moreo, Colossal magnetoresistant materials: the key role of phase separation, *Phys. Rep.* **344**, 1-153 (2001).

[16] Y. Tokura, Critical features of colossal magnetoresistive manganites, *Rep. Prog. Phys.* **69**, 797 (2006).

[17] Y. Shimakawa, Y. Kubo, and T. Manako, Giant magnetoresistance in $\text{Ti}_2\text{Mn}_2\text{O}_7$ with the pyrochlore structure, *Nature* **379**, 53-55 (1996).

[18] P. Majumdar and P. Littlewood, Magnetoresistance in Mn Pyrochlore: Electrical Transport in a Low Carrier Density Ferromagnet, *Phys. Rev. Lett.* **81**, 1314-1317 (1998).

[19] P. Rosa, Y. Xu, M. Rahn, J. Souza, S. Kushwaha, L. Veiga, A. Bombardi, S. Thomas, M. Janoschek, E. Bauer et al., Colossal magnetoresistance in a nonsymmorphic antiferromagnetic insulator, *Npj Quantum Materials* **5**, 52 (2020).

[20] Z.-C. Wang, J. D. Rogers, X. Yao, R. Nichols, K. Atay, B. Xu, J. Franklin, I. Sochnikov, P. J. Ryan, D. Haskel et al., Colossal Magnetoresistance without Mixed Valence in a Layered Phosphide Crystal, *Adv. Mater.* **33**, 2005755 (2021).

[21] J. Yin, C. Wu, L. Li, J. Yu, H. Sun, B. Shen, B. A. Frandsen, D.-X. Yao, and M. Wang, Large negative magnetoresistance in the antiferromagnetic rare-earth dichalcogenide EuTe_2 , *Phys. Rev. Mater.* **4**, 013405 (2020).

[22] H. Yang, Q. Liu, Z. Liao, L. Si, P. Jiang, X. Liu, Y. Guo, J. Yin, M. Wang, Z. Sheng et al., Colossal angular magnetoresistance in the antiferromagnetic semiconductor EuTe_2 , *Phys. Rev. B* **104**, 214419 (2021).

- [23] Z. Sun, A. Wang, H. Mu, H. Wang, Z. Wang, T. Wu, Z. Wang, X. Zhou, and X. Chen, Field-induced metal-to-insulator transition and colossal anisotropic magnetoresistance in a nearly Dirac material EuMnSb_2 , *npj Quantum Mater.* **6**, 94 (2021).
- [24] C. Huang, M. Huo, X. Huang, H. Liu, L. Li, Z. Zhang, Z. Chen, Y. Han, L. Chen, F. Liang, H. Dong, B. Shen, H. Sun, and M. Wang, Tuning the colossal magnetoresistance in $(\text{Mn}_{1-x}\text{Mg}_x)_3\text{Si}_2\text{Te}_6$ by engineering the gap and magnetic properties via doping and pressure, *Phys. Rev. B* **109**, 205145 (2024).
- [25] J. Seo, C. De, H. Ha, J. E. Lee, S. Park, J. Park, Y. Skourski, E. S. Choi, B. Kim, G. Y. Cho et al., Colossal angular magnetoresistance in ferrimagnetic nodal-line semiconductors, *Nature* **599**, 576-581 (2021).
- [26] A. May, Y. Liu, S. Calder, D. Parker, T. Pandey, E. Cakmak, H. Cao, J. Yan, and M. McGuire, Magnetic order and interactions in ferrimagnetic $\text{Mn}_3\text{Si}_2\text{Te}_6$, *Phys. Rev. B* **95**, 174440 (2017).
- [27] Y. Ni, H. Zhao, Y. Zhang, B. Hu, I. Kimchi, and G. Cao, Colossal magnetoresistance via avoiding fully polarized magnetization in the ferrimagnetic insulator $\text{Mn}_3\text{Si}_2\text{Te}_6$, *Phys. Rev. B* **103**, L161105 (2021).
- [28] Y. Zhang, Y. Ni, H. Zhao, S. Hakani, F. Ye, L. DeLong, I. Kimchi, and G. Cao, Control of chiral orbital currents in a colossal magnetoresistance material, *Nature* **611**, 467-472 (2022).
- [29] Y. Zhang, L. Lin, A. Moreo, and E. Dagotto, Electronic structure, magnetic properties, spin orientation, and doping effect in $\text{Mn}_3\text{Si}_2\text{Te}_6$, *Phys. Rev. B* **107**, 054430 (2023).
- [30] R. A. Susilo, C. I. Kwon, Y. Lee, N. P. Salke, C. De, J. Seo, B. Kang, R. J. Hemley, P. Dalladay-Simpson, Z. Wang, D. Y. Kim, K. Kim, S. W. Cheong, H. W. Yeom, K. H. Kim, and J. S. Kim, High-temperature concomitant metal-insulator and spin-reorientation transitions in a compressed nodal-line ferrimagnet $\text{Mn}_3\text{Si}_2\text{Te}_6$, *Nat Commun.* **15**, 3998 (2024).
- [31] Y. Zhang, Y. Ni, P. Schlottmann, R. Nandkishore, L. DeLong, and G. Cao, Current-sensitive Hall effect in a chiral-orbital-current state, *Nature Communications* **15**, 3579 (2024).
- [32] Z. Zhang, G. Liu, W. Qi, H. Xie, J. Guo, Y. Du, T. Wang, H. Zhang, F. Zhou, J. Li, Y. Zhang, Y. Yu, F. Fei, X. Xi, and F. Song, Variation of magnetic properties with current in ferrimagnetic semiconductor $\text{Mn}_3\text{Si}_2\text{Te}_6$, *AIP Advances* **14**, 035238 (2024).
- [33] S. W. Lovesey, Anapole, chiral, and orbital states in $\text{Mn}_3\text{Si}_2\text{Te}_6$, *Phys. Rev. B* **107**, 224410 (2023).
- [34] G. Sala, J. Lin, A. Samarakoon, D. Parker, A. May, and M. Stone, Ferrimagnetic spin waves in honeycomb and triangular layers of $\text{Mn}_3\text{Si}_2\text{Te}_6$, *Phys. Rev. B* **105**, 214405 (2022).
- [35] J. Wang, S. Wang, X. He, Y. Zhou, C. An, M. Zhang, Y. Zhou, Y. Han, X. Chen, J. Zhou, and Z. Yang, Pressure engineering of colossal magnetoresistance in the ferrimagnetic nodal-line semiconductor $\text{Mn}_3\text{Si}_2\text{Te}_6$, *Phys. Rev. B* **106**, 045106 (2022).
- [36] C. Ran, X. Mi, J. Shen, H. Wang, K. Yang, Y. Liu, G. Wang, G. Wang, Y. Shi, A. Wang, Y. Chai, X. Yang, M. He, X. Tong, and X. Zhou, Anomalous Nernst effect and topological Nernst effect in the ferrimagnetic nodal-line semiconductor $\text{Mn}_3\text{Si}_2\text{Te}_6$, *Phys. Rev. B* **108**, 125103 (2023).
- [37] S. Chikazumi, Physics of Magnetism, Wiley, New York, 1964, p. 274.
- [38] T. Kahmann, E. L. Rösch, K. Enpuku, T. Yoshida, F. Ludwig, Determination of the effective anisotropy constant of magnetic nanoparticles - Comparison between two approaches, *Journal Of Magnetism And Magnetic Materials* **519** pp. 167402 (2021).
- [39] N. S. Akulov, On the course of the magnetization curve in strong fields, *Z. Physik* **69**, 822-831 (1931).
- [40] L. Néel, Relationship between the anisotropy constant and the saturation approach law of ferromagnets, *J. Phys. Radium* **9**, 193-199 (1948).
- [41] H. Hauser, D.C. Jiles, Y. Melikhov, L. Li, R. Grössinger, An approach to modeling the dependence of magnetization on magnetic field in the high field regime, *Journal Of Magnetism And Magnetic Materials* **300**, 273-283 (2006).
- [42] H. Vincent, D. Leroux, D. Bijaoui, R. Rimet and C. Schlenker, Crystal structure of $\text{Mn}_3\text{Si}_2\text{Te}_6$, *Journal Of Solid State Chemistry* **63**, 349-352 (1986).
- [43] F. Ye, M. Matsuda, Z. Morgan, T. Sherline, Y. Ni, H. Zhao, and G. Cao, Magnetic structure and spin fluctuations in the colossal magnetoresistance ferrimagnet $\text{Mn}_3\text{Si}_2\text{Te}_6$, *Phys. Rev. B* **106**, L180402 (2022).
- [44] Y. Liu, Z. Hu, M. Abeykoon, E. Stavitski, K. Attenkofer, E. D. Bauer, and C. Petrovic, Polaronic transport and thermoelectricity in $\text{Mn}_3\text{Si}_2\text{Te}_6$ single crystals, *Phys. Rev. B* **103**, 245122 (2021).
- [45] C. Bigi, L. Qiao, C. Liu, P. Barone, M. C. Hatnean, G. R. Siemann, B. Achinuq, D. A. Mayoh, G. Vinai, V. Polewczyk, D. Dagur, F. Mazzola, P. Bencok, T. Hesjedal, G. Laan, W. Ren, G. Balakrishnan, S. Picozzi, and P. D. C. King, Covalency, correlations, and interlayer interactions governing the magnetic and electronic structure of $\text{Mn}_3\text{Si}_2\text{Te}_6$, *Phys. Rev. B* **108**, 054419 (2023).
- [46] C. I. Kwon, K. Kim, S. Y. Kim, R. A. Susilo, B. Kang, K. Kim, D. Y. Kim, J. Kim, B. Kim, and J. S. Kim, Raman signatures of spin-phonon coupling in a self-intercalated van der Waals magnet $\text{Mn}_3\text{Si}_2\text{Te}_6$, *Current Applied Physics* **53**, 51-55 (2023).
- [47] S. Djurdjic Mijin, A. Šolajic, J. Pešić, Y. Liu, C. Petrovic, M. Bockstedte, A. Bonanni, Z. V. Popovic, and N. Lazarevic, Spin-phonon interaction and short-range order in $\text{Mn}_3\text{Si}_2\text{Te}_6$, *Phys. Rev. B* **107**, 054309 (2023).